Extragalactic H I Survey with FAST: First Look at the Pilot Survey Results

Jiangang Kang[1,2,3,4], Ming Zhu[1,2], Mei Ai[1,2], Haiyang Yu[1,2,3] , and Chun Sun[1,2]

[1] National Astronomical Observatories, Chinese Academy of Sciences, Beijing 100101, China; kjg@nao.cas.cn, mz@nao.cas.cn
[2] CAS Key Laboratory of FAST, National FAST, National Astronomical Observatories, Chinese Academy of Sciences, Beijing 100101, China
[3] School of Astronomy and Space Science, University of Chinese Academy of Sciences, Beijing 100049, China
[4] Beijing Normal University, Beijing 100875, China

Abstract

We present the first data release of H I sources extracted from a pilot extragalactic survey using the Five-hundred-meter Aperture Spherical radio Telescope (FAST). We extracted sources from three-dimensional (3D) spectral data cubes datacubes to perform interactive searching and computing, yielding global parameters for each source, extending redshift ranges of H I emission up to $z = 0.04$. A total of 544 extragalactic H I sources has been detected by the pilot FAST H I drift scan survey covering part of the sky region in R.A. (R.A. or α) and decl. (decl. or δ) range $00^{\mathrm{h}}47^{\mathrm{m}} <$ R. A. (J2000) $< 23^{\mathrm{h}}22^{\mathrm{m}}$ and $+24° <$ decl. (J2000) $< +43°$. Of which, 528 sources are matched with optical counterparts via examination of digital optical survey databases collected from NED and Vizier data center, and 449 of them have optical velocities. Furthermore, we detect 36 galaxies with H I mass $< 10^8\, M_\odot$, which is significant for the study of low-mass systems in the local universe. We present catalogs for all H I detections with signal-to-noise ratio (S/N) greater than 5.1. The data are classified into four categories based on their S/N and baseline qualities, which are flagged with code 1 to 4: (1) 422 sources with S/N > 6.5; (2) 61 sources with $5.1 \lesssim$ S/N $\lesssim 6.5$; (3) 28 sources with relatively poor baselines; (4) 33 sources that are partly masked by strong radio frequency interferences (RFIs). In addition, we find 16 H I sources that have not been matched with any counterparts in the existing galaxy catalogs. This data release can provide guidance for the future extragalactic H I survey with FAST.

Key words: galaxies: formation – radio lines: galaxies – surveys – galaxies: distances and redshifts – radiation: dynamics – galaxies: evolution

1. Introduction

Neutral atomic hydrogen (H I) is one of the key tracers for studying the evolution of a galaxy and matter distribution in the universe. The hydrogen content in a galaxy is usually presented in three states: neutral molecular (H_2), neutral atomic (H I) and ionized (H II). H I is usually the major phase observed in the outer regions of galaxy disks (Warren et al. 2004; Begum et al. 2005; Heald et al. 2011; Koribalski et al. 2018). H I emissions are also detected in filaments, plumes and/or bridges, tracing the gravitational interactions with neighboring galaxies (Koribalski et al. 2003; Meyer et al. 2004; Pearson et al. 2016). For many H I rich galaxies, the H I disks of spirals are usually much more extended than the stellar disks, which make them highly susceptible to external forces such as tidal interactions, gas accretion, and ram pressure stripping, while providing fuel for star formation (Meurer 1996; Begum & Chengalur 2005; Serra et al. 2012; Bosma 2017; Koribalski et al. 2020). Therefore, the amount and extent of H I in galaxies vary significantly with environment (Cortese & Hughes 2009; Lemonias et al. 2013; Dénes et al. 2014; Stevens & Brown 2017).

Over the past decades, a number of H I surveys has been conducted to detect H I in the local universe (Koribalski et al. 2020), including the the H I Parkes All-Sky Survey (HIPASS; Staveley-Smith et al. 2000; Barnes et al. 2001; Meyer et al. 2004) in the southern hemisphere, the Northern HIPASS catalogue (NHICAT; Wong et al. 2006), and the Effelsberg Bonn H I Survey (EBHIS; Kerp et al. 2011) in northern hemisphere. The Arecibo Legacy Fast ALFA Survey (ALFALFA; Giovanelli et al. 2005a) provides improved spatial resolution and sensitivity over 7000 deg^2. These surveys have played a key role in mapping the H I distribution, revealing the gas properties of nearby galaxies and providing a valuable census of the cosmic H I content at low redshift (Jones et al. 2018a; Koribalski et al. 2020; Maddox et al. 2021). See Koribalski et al. (2020) for a review of the H I surveys.

As the current largest single dish radio telescope in the world, one of the key scientific goals of Five-hundred-meter Aperture Spherical radio Telescope (FAST) is to perform a blind extragalactic H I sky survey over a cosmologically significant volume to exploit its superior sensitivity and angular resolution (Nan et al. 2011). The FAST H I survey will enlarge the survey area to a solid angle of 23,000 deg^2 with the decl.

range of $-14°.3 <$ decl. $< +66°.7$ and up to a redshift of 0.35 to carry out a census of H I galaxies in the northern sky (Li et al. 2018; Jiang et al. 2019). As one of the long term key programs, the extragalactic H I survey is scheduled to be carried out simultaneously with several other projects (Galactic H I survey, pulsar search, fast radio burst search) in the Commensal Radio Astronomy FAST Survey (CRAFTS) with 19-beam receivers in the 1.05–1.45 GHz frequency range (*L* band) since 2020 (Li et al. 2018; Jiang et al. 2019). One of the key scientific goals of the FAST H I survey is to investigate the H I mass function (HIMF) at lower redshifts and its dependence on galaxy group and cluster environment. HIMF plays a key role in revealing the galactic evolution history as a function of redshift and explaining several crises between observations and simulations at small scales based on the Λ Cold Dark Matter (ΛCDM) model (Obreschkow et al. 2009; Duffy et al. 2012; Weinberg et al. 2015; Jones et al. 2018b). For instance, the slope at the faint end of HIMF (Springob et al. 2005a; Zwaan et al. 2005; Jones et al. 2018b) is still a puzzle, and various H I surveys measure an abundance of low-mass H I systems that is far less than the number of dark matter sub-halos inferred from numerical simulations (Briggs et al. 1997; Klypin et al. 1999; Rosenberg & Schneider 2000; Barnes et al. 2001; Giovanelli et al. 2005a; Nan et al. 2011; Zhang et al. 2019). With its superior sensitivity and large sky coverage, FAST should be able to detect thousands of low mass galaxies with H I masses less than $10^8 M_\odot$, and therefore will be able to increase the abundance of low mass H I galaxies and thus provide a viable solution to the "missing satellites" problem (Klypin et al. 1999; Moore et al. 1999; Giovanelli et al. 2005a; Strigari et al. 2007; Weinberg et al. 2015). In addition, according to recent observations, some of the Milky Way (MW) subhalos predicted by the ΛCDM model are significantly more massive than those resulting from stellar kinematics in its satellites, suggesting that the MW is missing a portion of subhalos, which is known as the "too big to fail" (TBTF) problem (Boylan-Kolchin et al. 2011, 2012). This phenomenon has been confirmed in the M31 environment (Tollerud et al. 2014) as well as in a population of field dwarfs (Ferrero et al. 2012; Papastergis et al. 2015), which indicates that this paradox has nothing to do with environmental effects. The simplest and most direct way to investigate the connection between observations and ΛCDM predictions is offered by the rotational velocity function (Peebles 2001; Giovanelli & Haynes 2015; Klypin et al. 2015). The dark matter halo mass function corresponds to the rotational velocity function of galaxies. The rotational velocity of a galaxy can be inferred from its velocity width of H I profile as the H I gas can extend further than any other directly observable component. A large number of galaxies is required to derive the H I velocity function and to tackle the TBTF problem (Baldry et al. 2008; Zwaan et al. 2010; Papastergis et al. 2011, 2013;

Cattaneo et al. 2014; Giovanelli & Haynes 2015; Ai & Zhu 2018; Zhang et al. 2020).

In order to test our ability to discriminate cosmic signals from radio frequency interference (RFI) and to optimize data-taking and calibration procedures, we have carried out a pilot H I survey. This paper presents the first data release from this pilot H I survey, in a catalog containing 544 H I detections from the northern sky region in $+24° < \delta < +43°$. Among them, 302 H I detections are also presented in the ALFALFA catalog over the same sky area at the range $+24 < \delta < +36°$ (Haynes et al. 2018), which enable us to make full comparison between the FAST and ALFALFA data sets. The FAST H I pilot survey was designed to cover a vast variety of cosmic environments, which includes several nearby over-density regions such as the Virgo Cluster and the Perseus-Pisces Supercluster (PPS) along with a large nearby cosmic void in its foreground (Saintonge et al. 2008).

The rest of the paper is organized as follows. In Section 2, we briefly introduce the key FAST survey parameters and describe sky area covered, give an overview of the FAST H I observing and data reduction processes and present a search for 544 H I detections. In Section 3, we present the results from the statistical properties of the sample and a description of these H I detections and 16 H I sources with no optical counterparts and discuss the implications of these galaxies. Finally in Section 4 we summarize this work. We assume H_0 (Hubble Constant) $= 70$ km s^{-1} Mpc^{-1}, Ω_m (density parameter of matter) $= 0.3$ and Ω_Λ (density parameter of dark energy) $= 0.7$ and we use natural unit for the speed of light throughout the paper.

2. The Data

2.1. Sky Coverage

Figure 1 presents the footprint of 71 discontinuous datacubes in this data release of the pilot H I survey. They are distributed in the range of $+24° < \delta < +43°$ and $00^h47^m < $ R. A. $< +24^h00^m$. These specific regions were selected for their moderate zenith angles so that both sensitivity and pointing accuracy of the telescope were optimized. We scan these sky regions over a large R.A. range, and to test the performance of all the FAST equipment in a variety of conditions during the pilot survey (Nan et al. 2011; Jiang et al. 2019; Zhang et al. 2020). In order to obtain some early science results, high density regions in the northern sky, such as the PPS, are targeted as a foremost sky region to study some important features of the local universe.

2.2. FAST Observations and Data Reduction

The data reported here were taken during the period of May 2020 to August 2021, and the pilot H I survey was carried out as a time-filler project when there were no other programs in
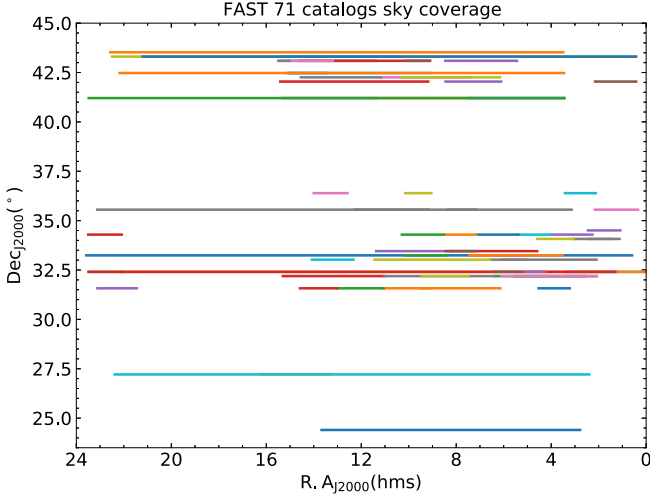
Figure 1. The 71 datacubes representing sky coverage for this catalog in a $+24° < \mathrm{decl.} < +43°$ decl. strip. Each decl. line width is about $20'-30'$.

the FAST observing queue. Although such type of project cannot be planned for specified targets, we can still do a blind search for H I emission. Our observational set-up was fixing the sky decl., and doing drift scans during the project time. Each scan lasted for about 1–8 hr. We also used some commissioning time to do calibration observations. The FAST H I survey is carried out with the drift scan mode employing FAST's focal-plane 19-beam receiver system, which is set in a hexagonal array and works in dual polarization mode, with a frequency range from 1050 to 1450 MHz. The 19-beam receiver was rotated by $23°.4$ so that the beam tracks were equally spaced in decl. with $1'.14$ spacing (Li et al. 2018). For the backend, we choose the Spec (W) spectrometer which has 65,536 channels covering the bandwidth of 500 MHz for each polarization and beam, with a velocity spacing of $1.67\ \mathrm{km\,s^{-1}}$ and a spectral resolution, after Hanning smoothing, of about $5\ \mathrm{km\,s^{-1}}$ which is sufficient for resolving fine spectral structure and obtaining accurate column densities and velocity fields.

The raw data output from each drift scan observation was reduced using a Python based data reduction pipeline HIFAST which was developed by Jing et al. (2022, in preparation). This pipeline consists of the following steps: (a) identify the calibration signal and calibrate the unit of the spectrum into kelvin. The calibration signal was from a standard 10 K noise diode which is injected every 32 s. The detailed procedure was described in Zhang et al. (2021); (b) convert the telescope pointing parameters to the precise position of R.A. and decl. for each spectrum; (c) subtract the baseline for each spectrum using the asymmetrically reweighted penalized least squares algorithm (Baek et al. 2015); (d) calibrate the flux unit from T_A kelvin to Jy using the conversion factor $16\ \mathrm{K\,Jy^{-1}}$ (Jiang et al. 2019); (e) correct the Earth's rotation and convert the redshift velocity from local standard of rest to the heliocentric velocity

in the equatorial coordinate system; (f) finally, create the three-dimensional (3D) datacubes consisting of R.A. and decl., and velocity in FITS data format. Once a data file is processed by the pipeline, the drift scan data were gridded to form 3D datacubes with $1'$ spacing. To limit the size of the datacube, the velocity coverage of the datacube for the pilot survey is limited to the range from -2000 to $19,000\ \mathrm{km\,s^{-1}}$.

Finally, we perform interactive search for H I emission lines in 71 datacubes as shown in Figure 1. The datacubes were displayed with the Starlink[5] software package and the H I emission sources were identified by human eyes and extracted manually. The final list of the H I catalog containing 544 sources is presented in Table 1.

2.3. Optical Counterparts of the H I Detections

For each H I detected source, we searched for its optical counterpart using the NED database. Fields of $4' \times 4'$ around each H I detection were inspected. The counterparts were usually found within a circle of $1'.5$ radius centered at the H I source position, and the offset between optical velocity and H I radio velocity was less than $300\ \mathrm{km\,s^{-1}}$ and the two redshifts were almost equal with error less than 0.001. Once optical sources were found within the search cone, we chose those sources with the type "G" standing for a galaxy in NED. Most of the best matched counterparts were found to be from various existing catalogs such as the UGC catalog, NGC/IC catalog,[6] WISE catalog,[7] 2MASS[8] catalog, KUG[9] catalog, MRK[10] catalog, SDSS[11] catalog, MGC[12] catalog, PGC[13] and GALEX[14] catalog, and CGCG.[15] We also found that 302 FAST detections had been detected by ALFALFA and reported in the Arecibo General Catalog (AGC).[16]

There are a few objects whose counterparts have not been attributed to the catalogs listed above, but they match the position and velocity of the FAST detected H I sources perfectly. These galaxies were found in the VizieR Online Data Catalog. Notes on individual galaxies are as listed in Table 1:

1. Col. 1: FAST galaxies catalog identification (FGC ID).
2. Col. 2: Optical counterpart identification (Optical ID) number for these catalog detections

---

5 http://starlink.eao.hawaii.edu/starlink
6 http://www.ngcicproject.org/
7 https://irsa.ipac.caltech.edu/frontpage/
8 http://egg.astro.cornell.edu/alfalfa/data/index.php
9 http://dbc.nao.ac.jp/cjads.html
10 https://heasarc.gsfc.nasa.gov/W3Browse/rosat/markarian.html
11 http://skyserver.sdss.org
12 https://heasarc.gsfc.nasa.gov/W3Browse/rosat/markarian.html
13 http://cseligman.com/text/atlas/pgcmisc.htm
14 http://www.galex.caltech.edu/researcher/data.html
15 https://heasarc.gsfc.nasa.gov/W3Browse/galaxy-catalog/uzc.html
16 http://egg.astro.cornell.edu/alfalfa/data/index.php

Table 1
H I Detections and Their Optical Counterparts Without Special Catalogs

| FGC ID	Optical ID	α_{J2000}(H I)	δ_{J2000}(H I)	α_{J2000}(Opt.)	δ_{J2000}(Opt.)	Position Offset (arcmin)	cz (FAST H I) (km s^{-1})	cz (counterpart H I) (km s^{-1})	Velocity Offset (km s^{-1})
(1)	(2)	(3)	(4)	(5)	(6)	(7)	(8)	(9)	(10)
83	[BKB95] 0242+4236B	2: 45: 56.40	42: 48: 18.00	$02^h45^m56^s$	$+42^d48^m605^s$	0.309	5039.3	5192.1	152.8
331	LSBCF508-03	13: 18: 5.76	24: 44: 2.40	$13^h18^m07^s\!.58$	$+24^d44^m31^s\!.20$	1.203	2725.3	2793.5	68.2
358	SBS1415+437	14 : 17 : 3.36	43 : 29 : 42.00	$14^h17^m01^s\!.408$	$+43^d30^m05^s\!.47$	1.13	637	616.1	20.9
376	[TSK2008]1251	15 : 15 : 5.04	42 : 4 : 48.00	$15^h15^m3^s\!.12$	$+42^d4^m22^s\!.80$	0.837	2388.8	2549.1	160.3
383	KKR 65	22 : 2 : 6.72	42 : 8 : 56.40	$22^h2^m6^s\!.00$	$+42^d8^m56^s\!.40$	0.143	4356.5	4426.3	69.8
388	LCSBS2687P	22 : 40 : 16.32	34 : 38 : 31.20	$22^h40^m14^s\!.79$	$+34^d38^m41^s\!.71$	0.976	8404.1	8295.2	108.9
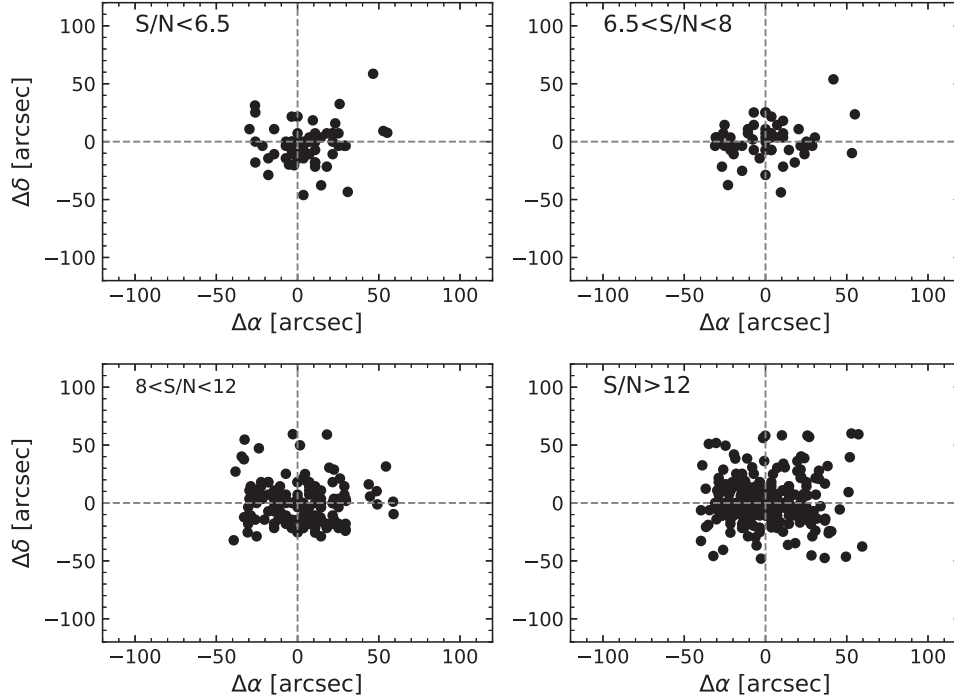
Figure 2. Pointing offsets between measured H I coordinates and the coordinates of the corresponding 527 optical counterparts in four different S/N bins, for which the mean pointing errors in (R.A., decl.) coordinates in the unit of arcsecond ($''$) are (19.4, 17.8), (20.5, 16.2), (21.6, 18.1) and (20.8, 20.1), respectively for the four plots from top-left to bottom-right.

3. Col. 3 and Col. 4: The R.A. and decl. of FAST galaxies.
4. Col. 5 and Col. 6: The R.A. and decl. of Optical counterpart.
5. Col.7: the position offset of FAST and optical counterparts.
6. Col.7 and Col 8: FAST source H I velocity and optical counterparts velocity.
7. Col.9: velocity offset between FAST and counterparts.

With the drift scan mode, most of the FAST observations are sampled at a fixed azimuth angle, and the zenith angle varies for different sources. To investigate possible dependence of the overall technical performance of the FAST telescope on pointing directions, we check the positional accuracy of the H I detections by comparing the H I detected position with the optical counterpart's position. The foremost key limitation factor for the positional accuracy of FAST sources is the resolution of the FAST beams, which are in an approximately circular shape, with half power beam widths of $2'.95$. The second key parameter affecting the quality of the FAST position accuracy is the signal-to-noise ratio (S/N) of the H I emission. High-S/N sources are located in more accurate centroids than those low-S/N ones. Positional accuracy can also be affected by other factors, including the systematic pointing offsets of the telescope, asymmetry in the H I profiles, centers of the optical and H I emission, statistical errors in the

H I sources and mismatch of optical counterparts. Figure 2 displays the position offsets between these H I sources and optical counterparts in the detected 527 sources, represented by black points. Each point stands for the offset of the optical source's R.A. and decl. coordinates from the center of the H I source coordinates in four different S/N panels. The average offset is about $20''$. Such accuracy is excellent considering the $2'.9$ size of the FAST beam. In the panel of S/N objects (S/N > 12), the mean position offsets for R.A. and decl. are $20''.8$ and $20''.1$, respectively. The velocity offset between counterpart and H I emission for 544 sources is within 300 km s^{-1} with the largest value being 218.6 km s^{-1} and the average is 94.7 km s^{-1}.

3. Results

3.1. Catalog Presentation

Here, we list 544 H I detections together with their optical counterparts in Table 2. The paper version lists 50 representative objects and the rest of the table is available online. These are detections acquired from 71 different datacubes with RFI and background level broadly removed. Table 3 shows 50 of 527 sources with optical counterparts that have optical redshift measurements, and the remaining H I sources and counterparts are available online. There are 16 sources that have no matched

Table 2
50 H I Detections with Optical Counterparts

FGC ID	Optical ID	α_{J2000}(H I)	δ_{J2000}(H I)	α_{J2000}(Opt.)	δ_{J2000}(Opt.)	$cz_\odot$ (km s^{-1})	W50 (km s^{-1})	F_{int} (Jy km s^{-1})	S/N	σ_{rms} (mJy)	Dist (Mpc)	$\log M_{H I}$ ($M_\odot$)	AGC ID	Code
(1)	(2)	(3)	(4)	(5)	(6)	(7)	(8)	(9)	(10)	(11)	(12)	(13)	(14)	(15)
1	UGC 12898	0 : 0 : 34.56	33 : 35 : 38.40	$0^h0^m37^s\!.44$	$+33^d36^m3^s\!.60$	4638.3	168.1	3.0	15.6	2	66.3	9.5		1
2	UGC 12920	0 : 2 : 23.04	27 : 12 : 10.80	$0^h2^m23^s\!.04$	$+27^d12^m39^s\!.60$	7319.4	276.5	3.0	18.9	1.5	104.6	10	12,920	1
3	UGC 00063	0 : 7 : 50.40	35 : 57 : 39.60	$0^h7^m50^s\!.88$	$+35^d57^m57^s\!.60$	450.0	73.3	3.6	18.3	2.8	6.4	7.4	63	3
4	UGC 00069	0 : 8 : 9.84	27 : 31 : 33.60	$0^h8^m11^s\!.04$	$+27^d31^m40^s\!.80$	4580.3	177.2	7.5	40.8	1.5	65.4	9.6	69	1
5	KUG0008+355	0 : 10 : 42.24	35 : 50 : 56.40	$0^h10^m41^s\!.76$	$+35^d50^m56^s\!.40$	6058.6	127.9	2.5	8.2	2.8	86.6	9.4	100,068	4
6	NGC 0021	0 : 10 : 48.00	33 : 20 : 24.00	$0^h10^m46^s\!.80$	$+33^d21^m10^s\!.80$	4865.4	349.4	1.0	7.7	2	69.5	9	100	1
7	UGC 00117	0 : 12 : 55.68	33 : 21 : 39.60	$0^h12^m54^s\!.48$	$+33^d21^m39^s\!.60$	4609.3	207.1	5.1	23.1	2	65.9	9.7	117	1
8	UGC 00128	0 : 13 : 51.60	35 : 59 : 16.80	$0^h13^m50^s\!.88$	$+35^d59^m38^s\!.40$	4469.2	216.7	10.8	28	2.8	63.9	9.8	128	1
9	WISEAJ001713.37 +271454.2	0 : 17 : 11.52	27 : 15 : 10.80	$0^h17^m13^s\!.20$	$+27^d14^m52^s\!.80$	3686.6	150.8	1.9	11.5	1.5	52.7	8.9	101,815	1
10		0 : 17 : 15.36	42 : 7 : 55.20			4844.4	215.7	4.6	16	2.7	69.2	9.7		1
11	UGC 00221	0 : 23 : 11.04	27 : 26 : 13.20	$0^h23^m10^s\!.80$	$+27^d25^m55^s\!.20$	3860.5	160.3	2.0	12.7	1.5	55.2	9.1	221	1
12	WISEAJ002638.16 +360018.7	0 : 26 : 36.48	35 : 59 : 52.80	$0^h26^m38^s\!.16$	$+36^d0^m18^s\!.00$	7179.3	143.9	1.3	5.7	2.8	102.6	9.2	104,539	3
13		0 : 28 : 32.40	33 : 15 : 50.40	$0^h28^m34^s\!.32$	$+33^d16^m19^s\!.20$	4570.7	214.2	4.0	17	2	65.3	9.6	284	1
14	UGC 00288	0 : 29 : 5.28	43 : 26 : 24.00	$0^h29^m3^s\!.60$	$+43^d25^m55^s\!.20$	197.1	49.1	2.5	15.7	3	3.8	7.3		3
15	UGC 00303	0 : 30 : 33.36	42 : 6 : 46.80	$0^h30^m31^s\!.68$	$+42^d6^m36^s\!.00$	5424.1	36.2	0.7	5.2	2.7	77.5	9		2
16	MRK0953	0 : 37 : 10.56	35 : 53 : 49.20	$0^h37^m12^s\!.24$	$+35^d54^m10^s\!.80$	4369.4	69.4	2.0	7.7	2.9	62.4	8.9	100,346	1
17	UGC 00376	0 : 37 : 54.72	32 : 41 : 13.20	$0^h37^m54^s\!.00$	$+32^d41^m20^s\!.40$	4734.9	205.7	8.4	30.7	1.9	67.6	10	376	1
18	UGC 00384	0 : 38 : 20.64	32 : 38 : 42.00	$0^h38^m22^s\!.08$	$+32^d38^m16^s\!.80$	4615.7	186.7	7.2	26.3	2.4	65.9	9.9	384	1
19	UGC 00394	0 : 38 : 43.92	42 : 0 : 18.00	$0^h38^m43^s\!.44$	$+41^d59^m49^s\!.20$	5393.5	60.8	0.8	5.4	2.7	77.1	9.1		1
20	NGC 0226	0 : 42 : 53.76	32 : 35 : 2.40	$0^h42^m54^s\!.00$	$+32^d34^m51^s\!.60$	4715.5	137.3	7.7	33.9	1.9	67.4	9.9	459	1
21	IC 0046	0 : 42 : 59.04	27 : 14 : 42.00	$0^h42^m58^s\!.08$	$+27^d15^m10^s\!.80$	5126.2	221.9	2.9	13.7	1.5	73.2	9.3	100,482	1
22	MRK0346	0 : 44 : 54.96	27 : 26 : 52.80	$0^h44^m56^s\!.88$	$+27^d26^m60^s\!.00$	5058.6	144.4	1.5	10.2	1.5	72.3	9.5	100,499	1
23	UGC 00484	0 : 46 : 57.36	32 : 40 : 1.20	$0^h46^m55^s\!.92$	$+32^d40^m30^s\!.00$	4795.0	408.2	15.1	40.7	1.9	68.5	10.2	484	1

Table 2
(Continued)

FGC ID	Optical ID	α_{J2000}(H I)	δ_{J2000}(H I)	α_{J2000}(Opt.)	δ_{J2000}(Opt.)	$cz_\odot$ (km s^{-1})	W50 (km s^{-1})	F_{int} (Jy km s^{-1})	S/N	σ_{rms} (mJy)	Dist (Mpc)	log $M_{H I}$ ($M_\odot$)	AGC ID	Code
(1)	(2)	(3)	(4)	(5)	(6)	(7)	(8)	(9)	(10)	(11)	(12)	(13)	(14)	(15)
24	KPG017	0 : 47 : 1.20	32 : 41 : 31.20	$0^h47^m3^s.12$	$+32^d41^m2^s.40$	4953.9	79.3	2.7	18.1	2.4	70.8	9.5	1730	1
25	UGC 00549	0 : 54 : 42.72	36 : 45 : 36.00	$0^h54^m42^s.00$	$+36^d45^m54^s.00$	6045.7	68.2	0.6	5.2	3.1	86.4	9		4
26	UGC 00602	0 : 58 : 21.36	36 : 44 : 16.80	$0^h58^m23^s.28$	$+36^d43^m48^s.00$	6126.2	212.5	2.3	9.4	2.9	87.5	9.6		4
27	MCG +07-03-013	1 : 00 : 54.96	43 : 41 : 6.00	$01^h00^m59^s.50$	$+43^d40^m26^s.0$	5000.6	200.1	2.2	8.5	3	71.4	9.4		1
28	KUG 0059+356	1 : 2 : 38.40	35 : 53 : 38.40	$1^h2^m39^s.60$	$+35^d53^m49^s.20$	2184.3	84.1	1.4	6.5	2.9	31.6	8.4	115,328	3
29	KUG 0108+356	1 : 11 : 34.56	35 : 52 : 8.46	$1^h11^m34^s.80$	$+35^d53^m20^s.40$	9446.6	129.0	1.5	6.3	2.9	135	9.7	115,609	4
30	KUG 0109+357	1 : 11 : 54.72	36 : 2 : 9.60	$1^h11^m52^s.80$	$+36^d1^m48^s.00$	9505.0	99.2	1.8	52.2	2.9	135.8	10	115,610	3
31		1 : 14 : 45.84	27 : 10 : 51.60			3570.7	100.0	5.0	22.1	1.5	51	8.8		1
32	CGCG502-074	1 : 24 : 9.84	32 : 45 : 28.80	$1^h24^m10^s.80$	$+32^d45^m57^s.60$	5871.7	147.4	2.3	10.8	2.2	83.9	9.6	110,302	1
33	NGC 0523	1 : 25 : 22.08	34 : 1 : 8.40	$1^h25^m20^s.64$	$+34^d1^m30^s.00$	4902.3	459.7	1.8	11.7	2.1	70	9.3	979	1
34	WISEAJ012622.06 +323806.9	1 : 26 : 20.40	32 : 38 : 24.00	$1^h26^m21^s.84$	$+32^d38^m9^s.60$	4079.8	63.8	1.0	6.2	2.4	58.3	8.9	115,203	1
35	NGC 0573	1 : 30 : 49.44	41 : 15 : 21.60	$1^h30^m49^s.44$	$+41^d15^m25^s.20$	2775.2	120.7	2.4	12.3	2.5	39.7	8.9		3
36	WISEAJ013141.69 +340858.2	1 : 31 : 42.48	34 : 8 : 56.40	$1^h31^m41^s.76$	$+34^d8^m60^s.00$	7095.5	59.8	0.8	6.1	2.1	101.4	9.3	115,595	1
37	WISEAJ013154.04 +271945.5	1 : 31 : 52.56	27 : 19 : 51.60	$1^h31^m54^s.00$	$+27^d19^m44^s.40$	3768.8	55.9	0.4	5.3	1.5	53.8	8.6	112,516	2
38	CGCG522-006	1 : 47 : 42.96	35 : 0 : 52.92	$1^h47^m43^s.68$	$+35^d1^m22^s.80$	5475.6	91.7	3.7	18.2	2.8	78.2	9.7	110,530	1
39	NGC 0672	1 : 47 : 54.48	27 : 25 : 51.60	$1^h47^m54^s.48$	$+27^d25^m58^s.80$	406.0	195.4	120.4	455.8	1.5	5.8	8.5	1256	1
40	CGCG482-017NED01	1 : 48 : 35.04	27 : 33 : 18.00	$1^h48^m35^s.28$	$+27^d32^m52^s.80$	10,473.9	131.5	2.4	15.3	1.5	149.6	9.8	110,534	1
41	IC 1731	1 : 50 : 12.48	27 : 11 : 52.80	$1^h50^m12^s.24$	$+27^d11^m45^s.60$	3536.9	174.8	6.7	26.9	1.5	50.5	9	1291	1
42	UGC 01347	1 : 52 : 45.36	36 : 36 : 43.20	$1^h52^m45^s.84$	$+36^d37^m8^s.40$	5467.6	138.3	3.4	12.8	2.9	78.1	9.7		1
43	UGC 01355	1 : 53 : 37.92	43 : 58 : 26.40	$1^h53^m36^s.24$	$+43^d57^m57^s.60$	6076.3	282.9	2.4	7.5	3	86.8	9.6		1
44		1 : 56 : 49.68	34 : 8 : 27.60			4739.3	385.4	2.7	18.4	2.1	67.7	9.5		1
45	WISEA J015708.84 +354852.0	1 : 57 : 9.60	35 : 48 : 54.00	$1^h57^m7^s.92$	$+35^d48^m25^s.20$	4441.9	181.7	2.7	8.8	2.9	63.5	9.3	115,626	1
46	UGC 01422	1 : 57 : 8.16	32 : 47 : 20.40	$1^h57^m6^s.72$	$+32^d47^m20^s.40$	4367.7	267.3	0.4	5.7	1.8	62.4	8.6	1422	2
47	NGC 0753	1 : 57 : 41.04	35 : 54 : 57.60	$1^h57^m42^s.24$	$+35^d54^m57^s.60$	4710.8	375.6	18.5	42.9	2.8	67.3	10	1437	1

Table 2
(Continued)

FGC ID	Optical ID	α_{J2000}(H I)	δ_{J2000}(H I)	α_{J2000}(Opt.)	δ_{J2000}(Opt.)	$cz_\odot$ (km s^{-1})	W50 (km s^{-1})	F_{int} (Jy km s^{-1})	S/N	σ_{rms} (mJy)	Dist (Mpc)	$\log M_{H I}$ ($M_\odot$)	AGC ID	Code
(1)	(2)	(3)	(4)	(5)	(6)	(7)	(8)	(9)	(10)	(11)	(12)	(13)	(14)	(15)
48	KUG 0156+324	1 : 59 : 7.92	32 : 43 : 30.00	$1^h59^m9\overset{s}{.}36$	$+32^d43^m4\overset{s}{.}80$	4304.9	168.9	5.1	26.6	1.8	61.5	9.7	115,273	1
49	UGC 01472	1 : 59 : 57.36	34 : 20 : 9.60	$1^h59^m58\overset{s}{.}90$	$+34^d20^m35\overset{s}{.}00$	4725.6	131.5	1.5	9	2.1	67.5	9.2	1472	1
50		2 : 6 : 30.96	43 : 51 : 36.00			5197.1	187.6	2.5	8.4	3	74.2	9.5		1

Table 3
50 H I Candidate Detections and Optical Counterparts

FGC ID	Optical ID	H I Velocity (Optical) (km s^{-1})	Optical Velocity (km s^{-1})	Magnitude (grb-band)	Galaxy Type
(1)	(2)	(3)	(4)	(5)	(6)
1	UGC 12898	4711.1	4780	16.5	G
2	UGC 12920	7502.4	7613	15.48	G
3	UGC 00063	450.7	441	15.34	G
4	UGC 00069	4651.4	4637	14.49	G
5	KUG0008+355	6183.4	6159	15.5	G
6	NGC 0021	4945.6	4765	13.51	G
7	UGC 00117	4681.2	4754	14.78	G
8	UGC 00128	4536.8	4531	16.5	G
10	WISEAJ001713.37+271454.2	3732.5	3704		G
12	UGC 00221	3910.9	3905	14.66	G
13	WISEAJ002638.16+360018.7	7355.3	7302		UvS
14	UGC 00284	4641.4	4732	14.71	G
15	UGC 00288	197.3	187	16	G
16	UGC 00303	5524.0	5623	16.5	G
17	MRK0953	4434.0	4441	15.5	G
18	UGC 00376	4810.8	4820	16	G
19	UGC 00384	4687.9	4702	14.43	G
20	UGC 00394	5492.3	5596	15.1	G
21	NGC 0226	4790.9	4830	14.31	G
22	IC 0046	5215.3	5286	14.75	G
23	MRK0346	5145.3	5186	16.5	G
24	UGC 00484	4872.9	4864	13.86	G
26	UGC 00549	6170.0	6062	15.79	G
27	UGC 00602	6253.9	6145	14.68	G
29	KUG 0059+356	2226.4	2205	16.5	G
30	KUG 0108+356	9753.7	9789	16.5	G
31	KUG 0109+357	9816.0	9741	17.5	G
33	CGCG502-074	5988.9	6024	15.6	G
34	NGC 0523	4983.8	4761	12.3B	G
35	WISEAJ012622.06+323806.9	4136.0	4135		UvES
36	NGC 0573	2801.1	2788	14.1	G
37	WISEAJ013141.69+340858.2	7267.4	7262		IrS
38	WISEAJ013154.04+271945.5	3816.7	3820		G
39	CGCG522-006	5577.4	5559	14.79	G
40	NGC 0672	406.6	429	11.47	G
41	CGCG482-017NED01	10,852.8	10,979	15.3	G
42	IC 1731	3579.1	3503	14	G
43	UGC 01347	5569.1	5543	13.49	G
44	UGC 01355	6201.9	6322	13.97	G
46	[DF2014] 01	4508.6	4592		G
47	UGC 01422	4432.3	4583	14.35	G
48	NGC 0753	4785.9	4858	12.97	G
49	KUG 0156+324	4367.6	4406	16.5	G
50	UGC 01472	4801.2	4849	16.07	G
52	UGC 01601	5483.9	5591	15.49	G
53	UGC 01602	5580.8	5489	16.5	G
54	UGC 01626	5497.2	5543	14.11	G
55	KUG 0206+355	4985.5	4973	16	G
56	UGC 01729	4492.0	4445	15.12	G
57	UGC 01738	5570.8	5686	15.48	G
58	IC 1784	5005.4	4817	14	G

Table 4
16 H I Candidate Detections With No Counterparts

FGC ID	α_{J2000}(H I)	δ_{J2000}(H I)	$cz_\odot$ (km s^{-1})	W50 (km s^{-1})	F_{int} (Jy km s^{-1})	S/N	σ_{rms} (mJy)	Dist (Mpc)	$\log M_{H I}$ ($M_\odot$)	Code	Note
(1)	(2)	(3)	(4)	(5)	(6)	(7)	(8)	(9)	(10)	(11)	(12)
10	00:17:15.34	42:07:56.85	4844.4	215.7	4.6	12	2.7	69.2	9.7	1	W
31	01:14:45.78	27:10:52.49	3570.7	100	5	11.7	1.5	51	8.8	1	S
44	01:56:49.57	34:08:27.17	4739.3	385.4	2.7	21	2.1	67.7	9.5	1	W
50	02:06:31.00	43:51:34.95	5197.1	187.6	2.5	6.8	3	74.2	9.5	1	W
78	02:43:16.03	36:39:57.10	5071.5	65.5	0.8	5.3	2.9	72.5	9	2	W
92	03:08:09.38	42:51:36.83	2553.2	25.9	1.1	22.6	2.4	36.5	8.5	1	S
93	03:08:35.36	36:27:17.10	3383.1	229	4	9.8	2.9	48.3	9.4	1	W
105	03:55:35.52	32:08:02.40	4135.9	40.2	0.7	10.2	2.9	59.1	8.8	1	W
121	04:52:18.91	32:24:42.31	3245.4	76.8	2.8	21.8	1.9	46.4	9.2	1	W
125	05:39:35.00	41:24:22.29	12,936	44.4	0.7	9.3	3.2	184.8	9.8	1	W
126	05:42:42.34	34:30:36.77	5918.4	74.8	3	14.7	2.9	84.6	9.7	1	W
127	05:51:15.75	43:22:24.11	3615.8	186.4	1.9	9.2	2.7	51.7	9.1	1	W
136	06:38:46.83	33:28:52.43	5002.2	49	0.8	5.7	2.6	71.5	9	2	W
138	06:43:20.56	42:26:04.06	6123	129.3	1.6	7.6	2.9	87.5	9.5	1	W
139	06:44:6.72	33 :21:36.00	7296.9	36.1	0.4	5.8	2.6	104.2	9.1	2	W
142	07:12:57.36	32 :13 48.00	4781.7	189.2	1.9	12.2	2	68.3	9.3	1	W

optical counterparts, which are listed in Table 4. The contents of the different columns in Tables 1 and 3 respectively are:

1. Col. 1: FAST galaxies catalog identification (FGC ID).
2. Col. 2: Optical counterpart identification (Optical ID) number for these catalog detections.
3. Cols. 3 and 4: Centroid position of each H I source in R. A. and decl., J(2000). The positional average accuracy is about 20″ and the accuracy of the H I positions depends on source emission intensity.
4. Cols. 5 and 6: J(2000) decl. and R.A. of the optical counterpart of the H I detection. Counterpart objects are examined based on spatial offset, morphology, galaxy type, magnitude, and velocity or redshift. If an H I source detection's optical counterpart cannot be found in the optical survey catalogs, the corresponding optical ID is kept empty.
5. Col. 7: Heliocentric redshift velocity of the H I sources, $cz_\odot$, taken at the midpoint between the channels where the flux density reaches its maximum value of the two flux peaks or one. Units are km s^{-1}.
6. Col. 8: Velocity width of the spectral line profile, W50, measured at the 50% level of the flux peaks, as in the description of Col. 6.
7. Col. 9: Integrated flux density of the source, F_c, in Jansky km s^{-1} (Jy km s^{-1}). This is measured on the integrated full spectral line after removing the baseline and background noise. Note that the uncertainty in the total flux calibration is about 10%, mostly due to the fact that no flux calibrators were measured during many of the drift scan observations, and we only use the average

conversion factor 16 K Jy^{-1} to convert from T_A scale to Jy scale.
8. Col. 10: S/N of the detection for integral flux, the error in integral flux for each source usually results from three parts: root mean square (rms) noise of each channel and the error from baseline fitting rms and integral range in line width W50. The total error is quantitatively estimated as $\sigma(F_c) = 4(S/N)_p^{-1}(F_p F_c \delta v)^{1/2}$ (Koribalski et al. 2004). The S/N for integral flux can be estimated with the format

$$S/N = \frac{F_c}{\sigma(F_c)}, \tag{1}$$

where F_c is the integral flux density in Jy km s^{-1}, $(S/N)_p = F_p/\sigma_{rms}$ is peak to noise ratio and δv is 5 km s^{-1} of velocity resolution.
9. Col. 11: Background noise rms of about 5 km s^{-1} velocity resolution with rebinned cubes per three channels.
10. Col. 12: Object distance in unit of megaparsecs (Mpc) from observational position, D_{Mpc}. The distance is simply cz/H_0; $cz_\odot$ is the recession velocity measured in the Cosmic Microwave Background reference frame and H_0 is the Hubble constant, for which we use a value of 70 km s^{-1} Mpc^{-1}.
11. Col. 13: $\log_{10}$ values of H I mass in solar unit of a source. That parameter is obtained using the expression $M_{H I} = 2.356 \times 10^5 D_{Mpc}^2 F_c$ (Giovanelli & Haynes 2015).
12. Col. 14: The corresponding entry number in the Arecibo General Catalog, a special database of extragalactic

objects maintained by M.P.H. and R.G. (Haynes et al. 2018), of these sources.

13. Col.15: Object code, sources with $(S/N)_p \geqslant 6.5$ are labeled code 1, sources with $5 \leqslant (S/N)_p < 6.5$ are recorded as code 2, and sources with relatively poor baselines or that are partly masked by strong RFIs are flagged with code 3 and 4, respectively.

In Table 3, we show the first 50 sources of 527 counterparts with basic parameters, for which column (1) to column (6) are FGC ID, optical ID, H I line velocity, optical velocity, apparent magnitude and object type, respectively. Here H I radio velocity has been transformed to optical velocity in column (3).

3.2. General Properties of the Detections

We first describe some basic properties of the 544 H I detections by FAST. About 28.9% of FAST detections have $cz < 3000$ km s^{-1}. The detection rate decreases when the FAST survey scans a sky region much larger than the supergalactic plane and extends to the low density environment outside the northern part of the Virgo Cluster. In this data release we did not include any sources that are in any doubt with regard to RFIs. Many tentative detections need to be confirmed with future observations and are not included in this catalog. Thus the H I detection rate with a single pass of drift scan is much lower than that of ALFALFA. We estimate a detection rate of about 0.8 per square degree for the pilot FAST survey area of about 681 square degrees, which is much lower than the average rate of 5.4 objects per square degree found in Haynes et al. (2018) where the survey area crosses the northern part of the Virgo Supercluster.

Figure 3 presents the distribution in values of heliocentric velocity cz, velocity width W50, S/N, and H I mass $M_{H I}$ for the H I detections in our catalog. The distances are inferred from redshifts along with the help of cosmic expansion dynamical theory. Due to the fact that many objects with less than 3000 km s^{-1} are likely to be located in the Virgo Cluster sky region or even the Local Group region, the model yields great uncertainties caused by the peculiar motions. Thus, the real distance could be different from that listed in Table 2. However, it would be easy to scale the data once a more reliable distance is obtained. Plot (e) indicates somewhat overabundance in the sources with H I mass less than $10^8 M_\odot$ in our catalog, which could be due to larger uncertainties in the distance measurements for nearby sources. Redshift-independent distance estimates of those objects are necessary, in order to obtain reliable determination of the HIMF in Virgo and in the field galaxies (Giovanelli et al. 2007).

The median redshift of the velocity distribution is 4681.33 km s^{-1}, which is just beyond the ridge of the PPS. The galaxies in this catalog have velocity widths W50 which vary from 24.9 to 539.3 km s^{-1} (see Figure 3). Some detected sources with narrow spectra turn out to be nearby dwarf galaxies with low H I masses. The upper limit is at 539.3 km s^{-1} for the line
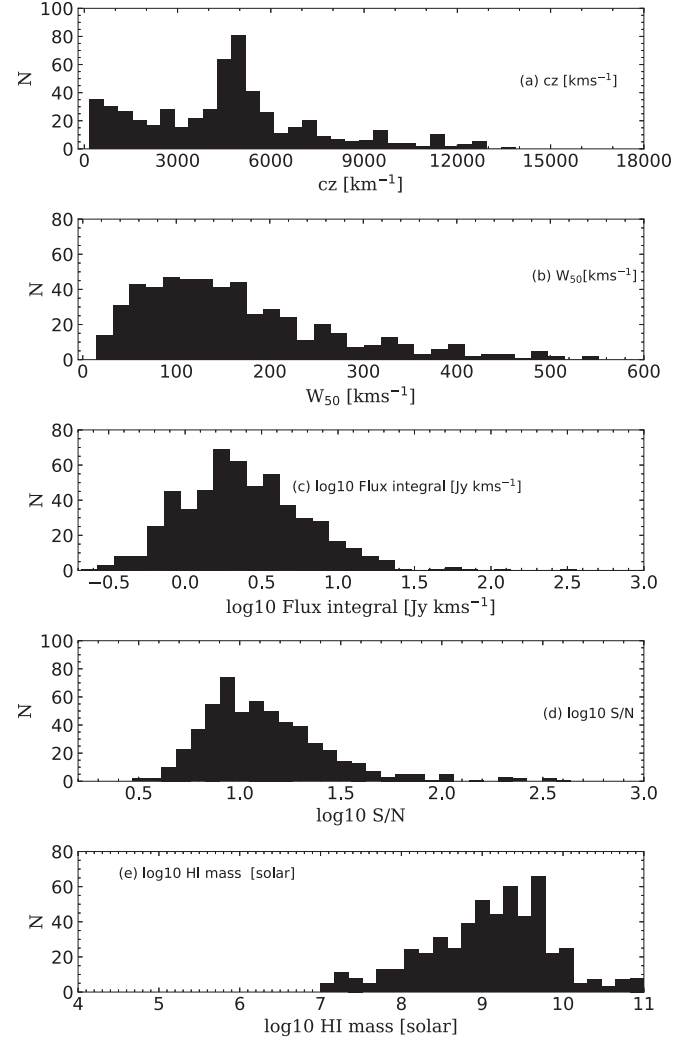
Figure 3. Histograms of the H I detections from top to bottom respectively: heliocentric recessional velocity in km s^{-1}, H I line width at half power (W50) in km s^{-1}, logarithm of the flux integral in Jy km s^{-1}, logarithm of the S/N, and logarithm of the H I mass in solar units.

width, close to the upper limit of the velocity width measured by previous H I samples (Koribalski et al. 2004; Springob et al. 2005b; Spekkens & Giovanelli 2006). It can also be seen that most of the line widths range from 100 to 200 km s^{-1}, the fraction of line width more than 300 km s^{-1} is significantly reduced and the largest line width is 539.3 km s^{-1}. The third panel of Figure 3 shows the integrated flux distribution. The distribution of fluxes ranges from 0.21 to 365.8 Jy km s^{-1}, and the median of the distribution is 2.3 Jy km s^{-1}. The S/Ns of the galaxies in Table 2 range from 5.1 to 436.8 with the lowest H I mass down to 7.1 logarithmic solar mass. As visible in the last panel of Figure 3, we found 36 galaxies with $\log_{10}(M_{H I}) < 8.0$ and the median of the mass distribution is $\sim 10^{9.2} M_\odot$, while the galaxy with the largest H I mass in this catalog is $\sim 10^{10.9} M_\odot$.
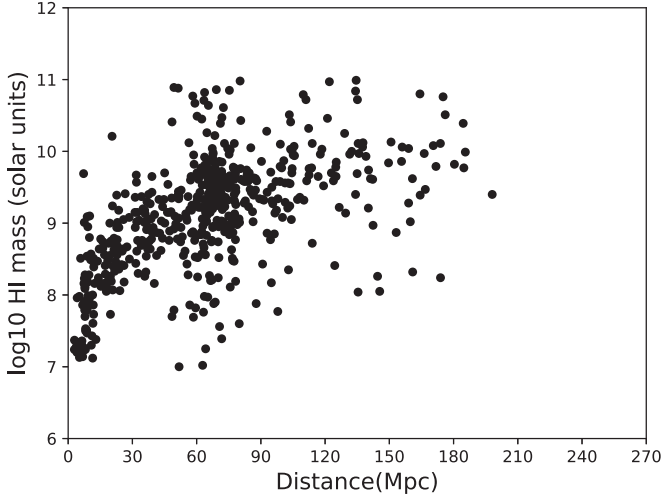
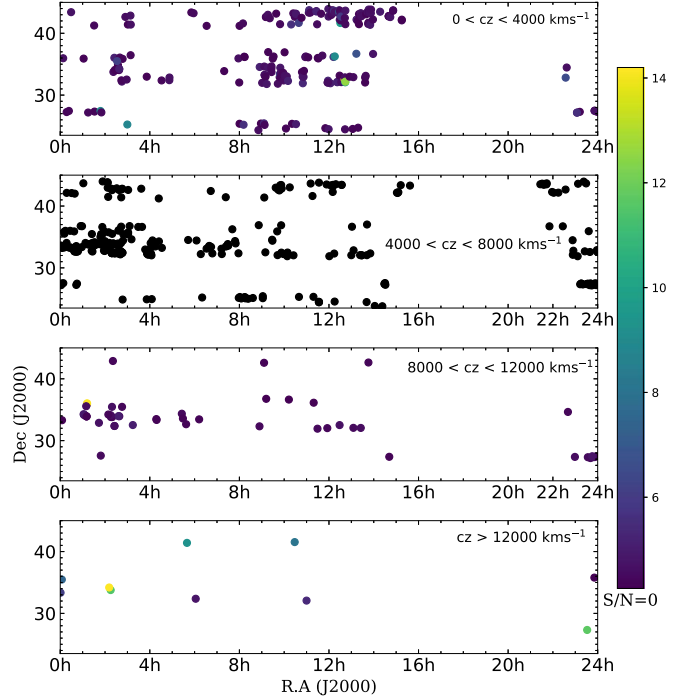**Figure 4.** Log distribution of measured H I mass as a function of recession distance.

Figure 5. The velocity distribution of all detections with the S/N in five different velocity cz intervals, presented as color scatters.

The distribution of the H I mass of the detections as a function of heliocentric recession velocity is presented in Figure 4. It confirms that 72.4% of 544 sources were detected within 120 Mpc and the farthest distance is 185.5 Mpc with H I mass about $10^{9.9}\,M_{\odot}$. There are 489 sources with H I mass less than $10^{10}\,M_{\odot}$.

Furthermore, we show the S/N distribution in different velocity bins for all detections in Figure 5. Some galaxies, such as FGC 30, FGC 39, FGC 87, FGC 209, FGC 314, FGC 318, FGC 321 and FGC 327, have very high S/N (>100), indicating that these galaxies have high H I fluxes. Some of them have very high H I masses, such as FGC 30, with a distance of 135.8 Mpc and H I mass of $10^{10}\,M_{\odot}$. In fact, a total of 55 gas rich galaxies has H I mass greater than $10^{10}\,M_{\odot}$. There are also many dwarf galaxies detected within the distance of 25 Mpc with H I mass larger than $10^{7}\,M_{\odot}$. The FAST H I survey will detect a large sample of this type of object with its superior sensitivity and efficiency, covering a variety of cosmic environments from voids to galaxy groups and clusters.

3.3. The Properties of the FAST Detections

The H I survey completeness can be defined as the fraction of cosmic sources of a given integrated flux density within the survey solid angle that are detected by a radio telescope (Giovanelli et al. 2005b). Although the sky coverage of the pilot survey is small, and the sky distributions of the datacubes are discontinuous, we can still try to get a sense of the completeness of the FAST survey.

Our results show that the spectral noise level at 5 km s^{-1} resolution is about 2.5 mJy on average, which reaches the expected sensitivity of FAST for the one-pass drift scan survey. The detection threshold of a given spectral profile depends on

both the shape and width of the profile. For wider profiles we can smooth the spectra further and the rms noise can decrease accordingly in term of the rms value of $2.5 \times (res/5)^{1/2}$ mJy, where res is the spectral resolution of the data after smoothing in units of km s^{-1}. The detection threshold (Giovanelli et al. 2005b) can be obtained with the formula

$$F_{\rm th} = ({\rm S/N}) \times ({\rm rms}) \times {\rm W50}, \qquad (2)$$

where S/N is a fiducial S/N value for a detection and rms is the rms background noise over a pixel after smoothing the spectrum, the noise rms is in unit of Jy and the width in km s^{-1}.

Assuming a critical parameter of 200 km s^{-1} as the threshold width, for the one-pass drift scan of the FAST survey, the empirical relationship between the integrated flux density detection threshold ($S_{\rm 21,th}$, in Jy km s^{-1}) and the profile width (W50, in km s^{-1}) from the pilot observations of FAST survey can be expressed in terms of the S/N as (Giovanelli et al. 2005b; Haynes et al. 2011)

$$S_{\rm 21,th} = \begin{cases} 0.11({\rm S/N}) \times ({\rm W50}/200)^{1/2}, & {\rm W50} < 200 \\ 0.11({\rm S/N}) \times ({\rm W50}/200), & {\rm W50} \geqslant 200. \end{cases} \qquad (3)$$

Note that the normalization factor of 0.11 here is different from that in Haynes et al. (2011) because the FAST data have a lower rms (2.5 mJy at 5 km s^{-1} resolution) than that of ALFALFA (3.5 mJy at 10 km s^{-1} resolution). It should also be
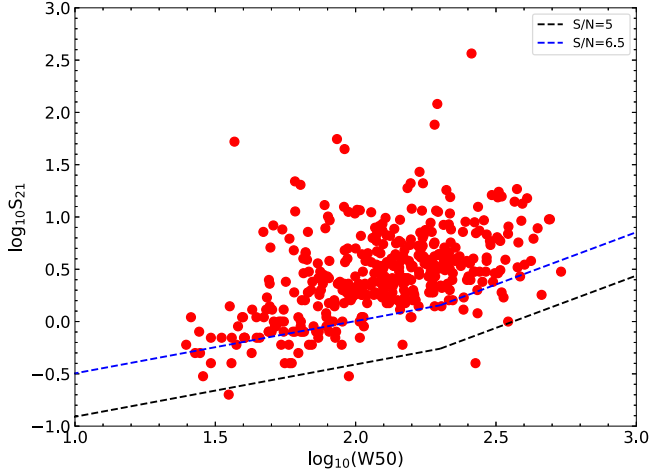
Figure 6. H I flux integral plotted vs. velocity width, for the detected sample. The two dashed lines correspond to the flux threshold F one obtains for an S/N of, respectively, 5 and 6.5, using Equation (3).
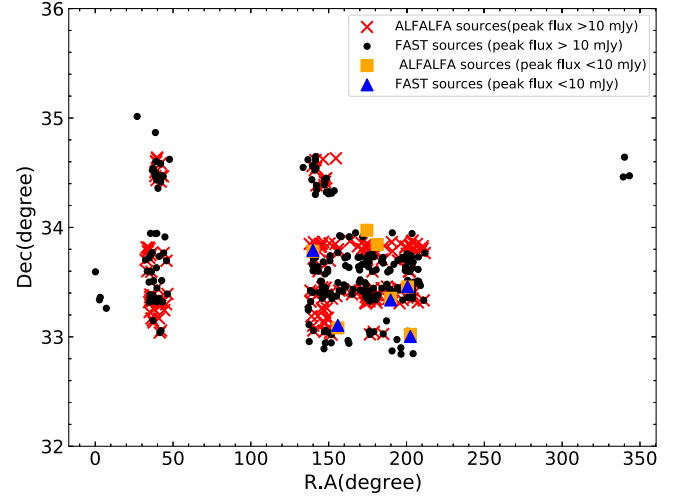

Figure 7. The comparisons of ALFALFA and FAST sources for decl. $33°$, $+34°.5$, red crosses represent ALFALFA sources and black solid dots mark FAST sources with a peak flux 10 mJy, while orange squares and blue triangles stand for ALFALFA and FAST sources with a peak flux of less than 10 mJy, respectively.

noted that there is about 10% uncertainty in the flux calibration for the pilot FAST survey data due to the lack of observation time for calibrator measurements.

Figure 6 displays a plot of the H I integrated fluxes of the H I detections versus their line width. This figure shows that the flux sensitivity limit of the survey depends on the velocity width. Lower fluxes can be detected for smaller line widths in Equation (3). The blue and black dashed lines in Figure 6 signify the possible detection thresholds at levels of S/N = 5 and 6.5, respectively. The median line width W50 for a typical galaxy is $143.56 \, \mathrm{km \, s^{-1}}$. The H I flux is positively correlated with the line width. The integrated H I flux traces the H I gas mass, while the line width traces the galaxy rotation curve which is related to the total mass of the galaxy. These two parameters are naturally correlated with each other because the H I mass is correlated with the total mass of the galaxy (Ai & Zhu 2018; Guo et al. 2020).

Since the data from the FAST pilot survey were reduced with an H I pipeline in-development, the RFI mitigation and standing wave removal depend heavily on human interactions. The automated source finding codes for the FAST survey are also under development, and the H I detections were identified by human eyes. Hence, it is possible that a few weak H I sources could be missed due to human mistakes or due to RFI contamination in the spectra. As affirmed in Figure 6, most of the detected sources have relatively high S/N (with S/N > 6.5). The sources with 5 < S/N < 6.5 are relatively rare, suggesting that the H I sources in this S/N range were not completely identified. In the next section we will further evaluate the completeness of our FAST detections by comparing with the ALFALFA data set.

3.4. Comparison with ALFALFA Detections

The ALFALFA survey relied on the seven-horn Arecibo L-band Feed Array (ALFA) to blindly survey nearly 7000 $\mathrm{deg^2}$ of high Galactic latitude sky over 4400 nighttime hours (Haynes et al. 2018). Of the 544 FAST detected sources, 302 of them are also detected by ALFALFA. Many of the FAST observed regions suffered serious RFI contamination, thus we chose two regions with less RFI effects to make a fair comparison with the ALFALFA data sets. Figure 7 compares the sources found in two declination ranges at $33°.02 <$ decl. $< 33°.9$ with $32°.2 <$ R. A. $< 212°$, and $33°.3 <$ decl. $< 34°.6$ with and $338°.5 <$ R. A. $< 48°.5$ and $137°.7 <$ R. A. $< 157°.5$. In these ranges, FAST detects 194 sources, while ALFALFA contains 204 sources satisfying common heliocentric velocity range $100 < cz < 13{,}000 \, \mathrm{km \, s^{-1}}$. The ALFALFA survey was conducted in two parts at $07^\mathrm{h}30^\mathrm{m} <$ R. A. $< 16^\mathrm{h}30^\mathrm{m}$ and $22^\mathrm{h} <$ R. A. $< 03^\mathrm{h}$ over $+0° <$ decl. $< +36°$. We found that more than 90% of the ALFALFA sources with peak flux more than 10 mJy are also detected by FAST. Of the seven ALFALFA sources with peak fluxes less than 10 mJy, five of them are detected by FAST. There are about 10%–20% of ALFALFA sources not detected by FAST due to RFI contamination.

Figure 7 demonstrates the FAST detection rate is slightly lower than that of ALFALFA for the regions we compared. The detection rate is much lower at the edge of the FAST scan maps due to lower sensitivity in these areas. Moreover, there are strong RFIs in the frequency range of 1100–1300 MHz which could impact the detection rate (Zhang et al. 2021). As a result,
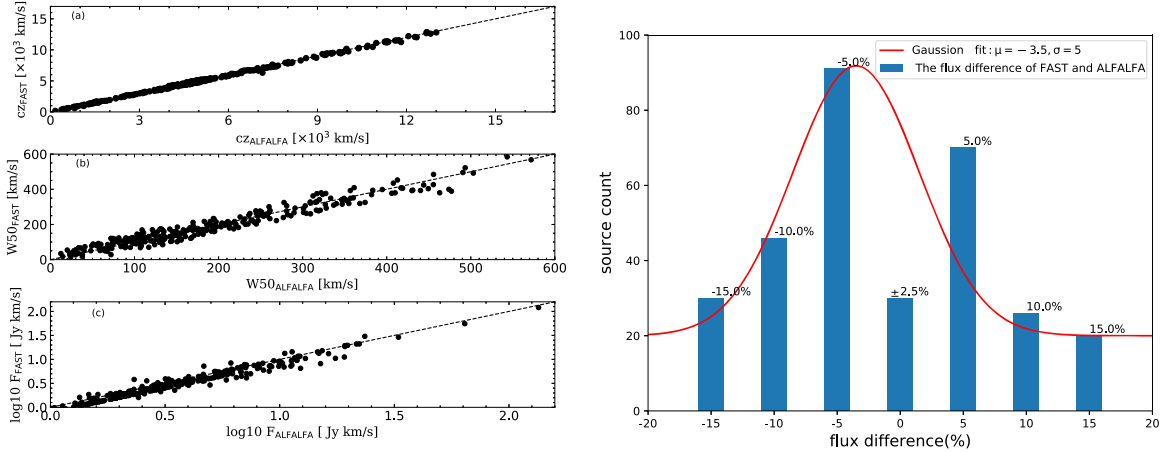
Figure 8. Left: Comparison between the properties of galaxies as measured by FAST and ALFALFA H I observations compiled by Haynes et al. (2018): (a) heliocentric recessional velocity in km s^{-1}, (b) H I velocity width at half of peak spectrum in km s^{-1}, and (c) logarithm of the flux integral in Jy km s^{-1}. Right panel: Bar chart for the flux difference in percentage for the sources detected by both FAST and ALFALFA.

the baselines are poor for some FAST sources, and some galaxies' spectra miss a part of the flux due to RFI masking.

To further check the telescope performance and our calibrations, we compare the FAST detected H I spectra with those of the ALFALFA survey. Figure 9 shows ten representative H I spectral profiles overlaid with the corresponding ALFALFA sources, where the x-axis labels the radio velocity in the unit of km s^{-1} and y-axis refers to the flux density in millijansky (mJy). The spectra measured with the FAST telescope match those from ALFALFA within 10% uncertainty. The FAST spectral resolution has been smoothed to 10 km s^{-1} to match that of ALFALFA (Haynes et al. 2018) and baseline fittings are generally good for all sources

$$\text{flux error } (\%) = \frac{Fc_{\text{FAST}} - Fc_{\text{ALFALFA}}}{Fc_{\text{FAST}}}. \quad (4)$$

Figure 8 in the left panel compares the ALFALFA measured values of velocity cz, line widths W50, and integrated fluxes F_c to those measured with the FAST H I drift scan observations for the 302 galaxies in common. The mean offsets are 57.5 km s^{-1} and 40.2 km s^{-1}, and the standard deviations are 121.6 km s^{-1} and 30.7 km s^{-1} for the cz and W50 measurements respectively. The FAST integrated fluxes are somewhat smaller than those measured with ALFALFA, which could be due to poor baseline fitting or affected by RFIs and standing waves. The flux difference estimated with Equation (4) for the 302 FAST-ALFALFA detected sources is presented as a bar chart in Figure 8, right panel. The flux differences are mostly ±15%. The mean offset μ and standard deviation σ for the Gaussian fit to the bar chart (Figure 8) are −3.5% and 5%, respectively. From these results, we find no significant difference between the FAST and ALFALFA data sets considering the

uncertainties in flux calibration for the pilot FAST H I survey which is about 10%.

3.5. H I Sources with No Optical Counterparts

Figures 10–17 present the H I spectra and intensity color maps for the 16 H I sources listed in Table 4, for which no optical counterparts have been matched. Four of these sources, e.g., FGC 10, FGC 31, FGC 44 and FGC 50, are located in regions not covered by current mainstream optical surveys, while other sources are within the optical survey area but they could be too faint to be detected by the optical surveys. It is possible that some H I detected sources are indeed optically dark galaxies, which have very low optical apparent magnitudes and are not detectable by optical telescopes. In Table 4, we mark the sources in the note column (12), where S stands for the sources that are too faint and beyond the SDSS survey detection limit of −22 mag in grz-band, while W signifies those beyond the WISE survey detection limit of −21 mag in W1/W2 band.[17] Other parameters in this table are identical to those of Table 2.

From Table 4 we can see that the H I sources without optical counterparts have an R.A. range from 0° to 110° with a maximum redshift of 0.024, and their H I masses vary from $10^{8.5}$ to $10^{9.7} M_\odot$. The total H I fluxes of these galaxies range from 0.7 to 5 Jy km s^{-1}, and their line widths range from 25.9 to 385.4 km s^{-1}. Based on the H I measurements of the fluxes and line widths, the gas properties of these optically "dark" galaxies appear to be normal. Future deep optical follow-up observations might be able to reveal some peculiar features in this type of galaxy.
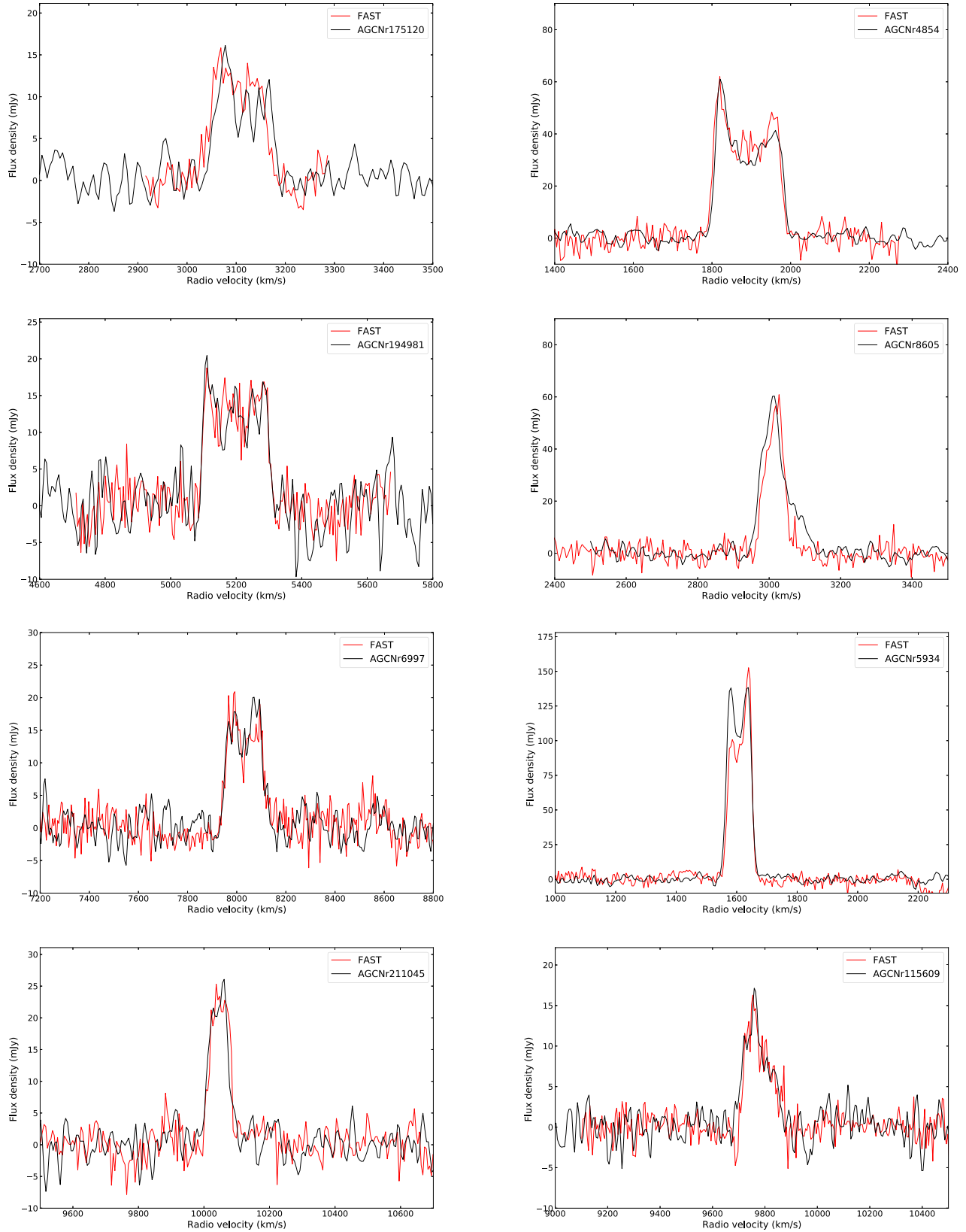
---

[17] https://www.legacysurvey.org/viewer/

Figure 9. Ten typical H I spectral lines of all the sources in the unit of Jy km s^{-1} for source flux at different radio velocity (km s^{-1}) ranges and overlapping corresponding ALFALFA source spectra.
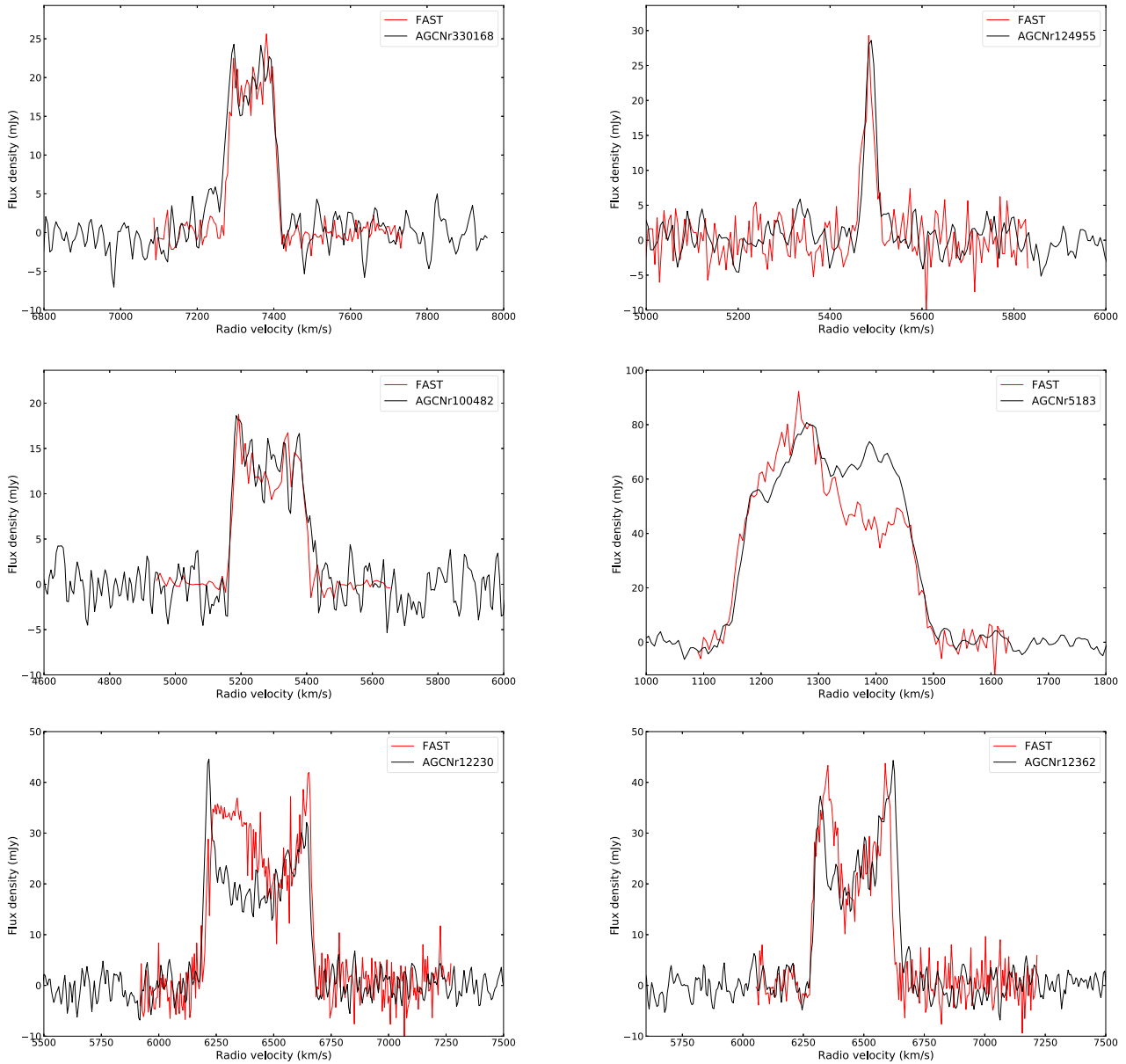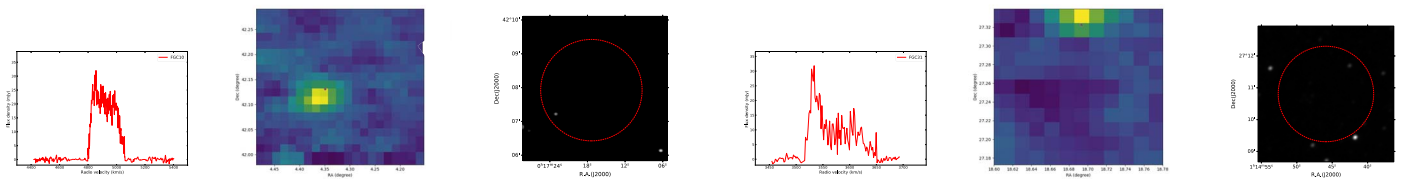
Figure 9. (Continued.)

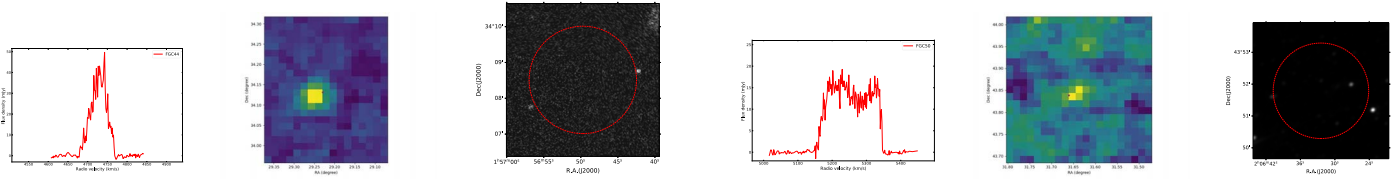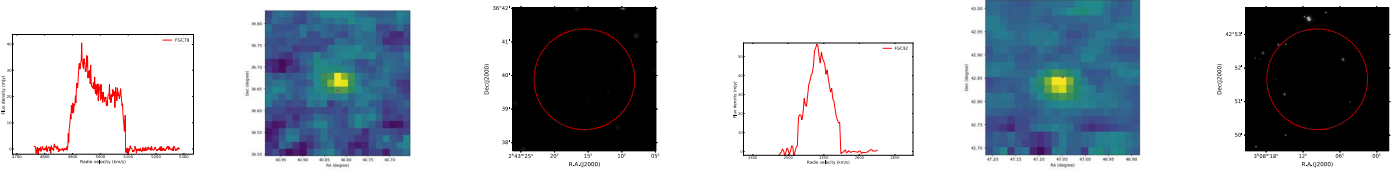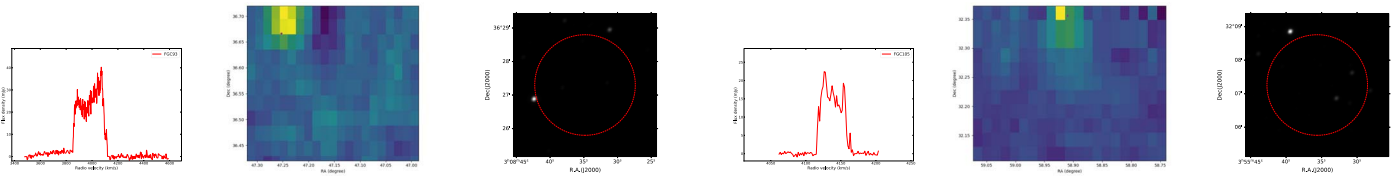**Figure 10.** Left and middle plots show H I source spectral line and H I intensity mappings, respectively, and their counterpart images in the SDSS *grz*-band in right panel. Left and middle plots display H I source spectral line and H I intensity mappings, respectively, and their counterpart images in unWISE W1/W2 NEO6 band in the right panels.
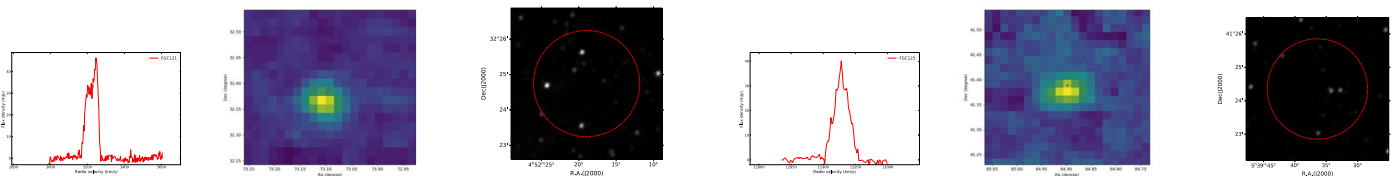
Figure 11. Left and middle plots show H I source spectral line and H I intensity mappings, respectively, and their counter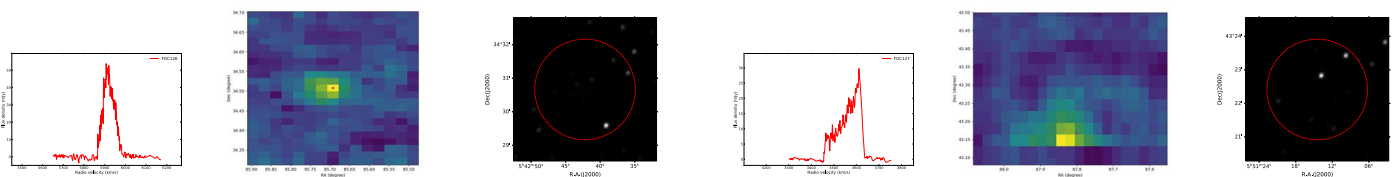part image in the unWISE W1/W2 NEO6 band in the right panel. Left and middle plots display H I source spectral line, H I intensity mappings, respectively, and their counterpart image in unWISE W1/W2 NEO6 band in the right panel.

Figure 12. Left and middle plots show H I source spectral line and H I intensity mappings, respectively, and their counterpart image in unWISE W1/W2 NEO6 band in right panel. Left and middle plots display the H I source spectral line and H I intensity mappings, respectively, and their counterpart image in the SDSS *grz*-band in the right panel.

Figure 13. Left and middle plots show H I source spectral line and H I intensity mappings, respectively, and their counterpart image in the unWISE W1/W2 NEO6 band in the right panel. Left and middle plots display H I source spectral line and H I intensity mappings, respectively, and their counterpart image in unWISE W1/W2 NEO6 band in the right panel.
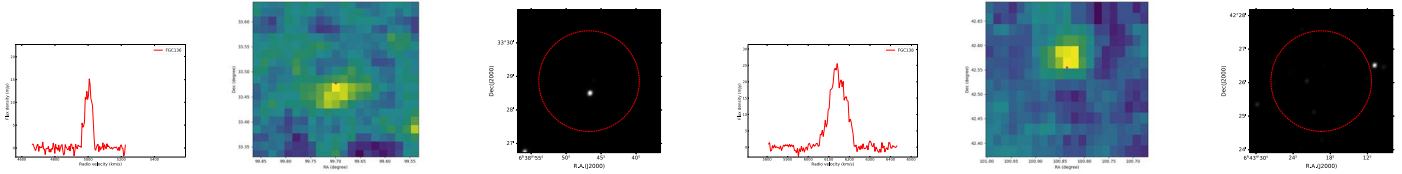

Figure 14. Left and middle plots show H I source spectral line and H I intensity mappings, respectively, and their counterpart image in unWISE W1/W2 NEO6 band in the right panel. Left and middle plots display the H I source spectral line and H I intensity mappings, respectively, and their counterpart image in the unWISE W1/W2 NEO6 band in the right panel.
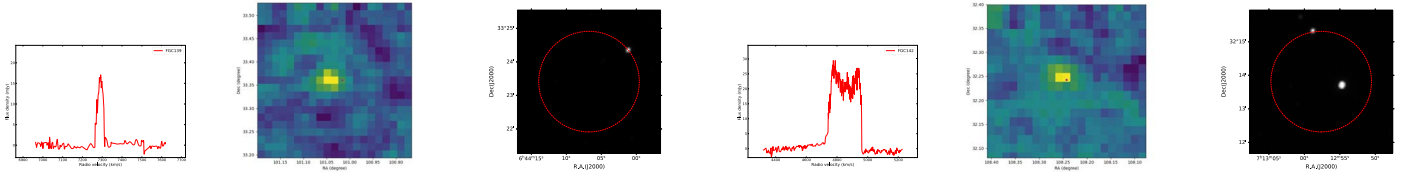

Figure 15. Left and middle plots show H I source spectral line and H I intensity mappings, respectively, and their counterpart image in the unWISE W1/W2 NEO6 band in the right panel. Left and middle plots display H I source spectral line and H I intensity mappings, respectively, and their counterpart image in the unWISE W1/W2 NEO6 band in the right panel.

Figure 16. Left and middle plots show H I source spectral line and H I intensity mappings, respectively, and their counterpart image in the unWISE W1/W2 NEO6 band in right panel. Left and middle plots display the H I source spectral line and H I intensity mappings, respectively, and their counterpart image in the unWISE W1/W2 NEO6 band in the right panel.

Figure 17. Left and middle plots show H I source spectrum line and H I intensity mappings, respectively, and their counterpart image in the unWISE W1/W2 NEO6 band in the right panel. Left and middle plots display H I source spectral line and H I intensity mappings, respectively, and their counterpart image in unWISE W1/W2 NEO6 band in the right panel.

4. Summary

We present a catalog of 544 H I detections from the FAST pilot H I survey in decl. range of $+24° < \delta < +43°$. All these sources were identified as extragalactic objects with $cz > 100$ and 527 of these sources can be matched with optical counterparts in online data archives. These detections are measured with a high confidence level in the accuracy of position and redshift measurements. In the catalog, we have classified these sources into four categories based on their S/N and baseline qualities. Among them, 302 sources are also detected by ALFALFA. In regions not affected by RFI and standing waves, the FAST measured H I fluxes and profiles are in general consistent with those of ALFALFA. More than 90% of ALFALFA detected sources with peak flux larger than 10 mJy were also detected in the FAST pilot H I survey. About 10%–20% sources were missed due to RFI contamination. More than 90% of the objects have $\log_{10}(M_{\rm H I}) < 10$ and 36 of them have $\log_{10}(M_{\rm H I}) < 8$. The fraction of sources with S/N > 6.5 is 89.3%. Our pilot study found 16 new H I detections without optical counterparts in redshift range $z < 0.024$. Some of them are quite massive in H I gas, but their optical fluxes could be too small to be detected in optical wavelengths. These objects feature a few peculiar physical characteristics that deserve further studies with multi-wavelength follow-up observations.

ORCID iDs

Haiyang Yu ⓘ https://orcid.org/0000-0001-9838-7159

References

Ai, M., & Zhu, M. 2018, ApJ, 862, 48
Baek, S. K., Park, H. J., & Kim, B. J. 2015, EPJB, 88, 127
Baldry, I. K., Glazebrook, K., & Driver, S. P. 2008, MNRAS, 945
Barnes, D. G., Staveley-Smith, L., de Blok, W. J. G., et al. 2001, MNRAS, 322, 486
Begum, A., & Chengalur, J. N. 2005, MNRAS, 362, 609
Begum, A., Chengalur, J. N., & Karachentsev, I. D. 2005, A&A, 433, L1
Bosma, A. 2017, in Formation and Evolution of Galaxy Outskirts, Proc. Int. Astronomical Union, IAU Symp., Vol. 321, ed. A. Gil de Paz, J. H. Knapen, & J. C. Lee, 220
Boylan-Kolchin, M., Bullock, J. S., & Kaplinghat, M. 2011, MNRAS: Letters, 415, L40
Boylan-Kolchin, M., Bullock, J. S., & Kaplinghat, M. 2012, MNRAS, 422, 1203
Briggs, F. H., Sorar, E., Kraan-Korteweg, R. C., & van Driel, W. 1997, PASA, 14, 37
Cattaneo, A., Salucci, P., & Papastergis, E. 2014, ApJ, 783, 66
Cortese, L., & Hughes, T. M. 2009, MNRAS, 400, 1225
Dénes, H., Kilborn, V. A., & Koribalski, B. S. 2014, MNRAS, 444, 667
Duffy, A. R., Meyer, M. J., Staveley-Smith, L., et al. 2012, MNRAS, 426, 3385

Ferrero, I., Abadi, M. G., Navarro, J. F., Sales, L. V., & Gurovich, S. 2012, MNRAS, 425, 2817

Giovanelli, R., & Haynes, M. P. 2015, A&ARv, 24

Giovanelli, R., Haynes, M. P., Kent, B. R., et al. 2005a, AJ, 130, 2598

Giovanelli, R., Haynes, M. P., Kent, B. R., et al. 2005b, AJ, 130, 2613

Giovanelli, R., Haynes, M. P., Kent, B. R., et al. 2007, AJ, 133, 2569

Guo, H., Jones, M. G., Haynes, M. P., & Fu, J. 2020, ApJ, 894, 92

Haynes, M. P., Giovanelli, R., Kent, B. R., et al. 2018, ApJ, 861, 49

Haynes, M. P., Giovanelli, R., Martin, A. M., et al. 2011, AJ, 142, 170

Heald, G., Allan, J., Zschaechner, L., et al. 2011, in Tracing the Ancestry of Galaxies, Vol. 277 ed. C. Carignan, F. Combes, & K. C. Freeman, 59

Jiang, P., Yue, Y., Gan, H., et al. 2019, Commissioning Progress of the FAST, arXiv:1903.06324

Jones, M. G., Espada, D., Verdes-Montenegro, L., et al. 2018a, A&A, 609, A17

Jones, M. G., Haynes, M. P., Giovanelli, R., & Moorman, C. 2018b, MNRAS, 477, 2

Kerp, J., Winkel, B., Ben Bekhti, N., Flöer, L., & Kalberla, P. 2011, AN, 332, 637

Klypin, A., Karachentsev, I., Makarov, D., & Nasonova, O. 2015, MNRAS, 454, 1798

Klypin, A., Kravtsov, A. V., Valenzuela, O., & Prada, F. 1999, ApJ, 522, 82

Koribalski, B., Gordon, S., & Jones, K. 2003, MNRAS, 339, 1203

Koribalski, B. S., Staveley-Smith, L., Kilborn, V. A., et al. 2004, AJ, 128, 16

Koribalski, B. S., Staveley-Smith, L., Westmeier, T., et al. 2020, Ap&SS, 365, 118

Koribalski, B. S., Wang, J., Kamphuis, P., et al. 2018, MNRAS, 478, 1611

Lemonias, J. J., Schiminovich, D., Catinella, B., Heckman, T. M., & Moran, S. M. 2013, ApJ, 776, 74

Li, D., Wang, P., Qian, L., et al. 2018, IMMag, 19, 112

Maddox, N., Frank, B. S., Ponomareva, A. A., et al. 2021, A&A, 646, 35

Meurer, G. 1996, Star Clusters And The Duration Of Starbursts, HST Proposal

Meyer, M. J., Zwaan, M. A., Webster, R. L., et al. 2004, yCat, VIII/73

Moore, B., Ghigna, S., Governato, F., et al. 1999, ApJL, 524, L19

Nan, R., Li, D., Jin, C., et al. 2011, IJMPD, 20, 989

Obreschkow, D., Croton, D., De Lucia, G., Khochfar, S., & Rawlings, S. 2009, ApJ, 698, 1467

Papastergis, E., Giovanelli, R., Haynes, M. P., Rodríguez-Puebla, A., & Jones, M. G. 2013, ApJ, 776, 43

Papastergis, E., Giovanelli, R., Haynes, M. P., & Shankar, F. 2015, A&A, 574, A113

Papastergis, E., Martin, A. M., Giovanelli, R., & Haynes, M. P. 2011, ApJ, 739, 38

Pearson, S., Besla, G., Putman, M. E., et al. 2016, MNRAS, 459, 1827

Peebles, P. J. E. 2001, ApJ, 557, 495

Rosenberg, J. L., & Schneider, S. E. 2000, in ASP Conf. Ser. 218, Mapping the Hidden Universe: The Universe behind the Milky Way—The Universe in HI, ed. R. C. Kraan-Korteweg, P. A. Henning, & H. Andernach (San Francisco, CA: ASP), 223

Saintonge, A., Giovanelli, R., Haynes, M. P., et al. 2008, AJ, 135, 588

Serra, P., Oosterloo, T., Morganti, R., et al. 2012, MNRAS, 422, 1835

Spekkens, K., & Giovanelli, R. 2006, AJ, 132, 1426

Springob, C. M., Haynes, M. P., & Giovanelli, R. 2005a, ApJ, 621, 215

Springob, C. M., Haynes, M. P., Giovanelli, R., & Kent, B. R. 2005b, yCat, VIII/77

Staveley-Smith, L., Koribalski, B. S., Stewart, I., et al. 2000, in ASP Conf. Ser. 217, Imaging at Radio through Submillimeter Wavelengths, ed. J. G. Mangum & S. J. E. Radford (San Francisco, CA: ASP), 50

Stevens, A. R. H., & Brown, T. 2017, MNRAS, 471, 447

Strigari, L. E., Bullock, J. S., Kaplinghat, M., et al. 2007, ApJ, 669, 676

Tollerud, E. J., Boylan-Kolchin, M., & Bullock, J. S. 2014, MNRAS, 440, 3511

Warren, B. E., Jerjen, H., & Koribalski, B. S. 2004, in Dark Matter in Galaxies, Vol. 220 ed. S. Ryder et al., 369

Weinberg, D. H., Bullock, J. S., Governato, F., Kuzio de Naray, R., & Peter, A. H. G. 2015, PNAS, 112, 12249

Wong, O. I., Ryan-Weber, E. V., Garcia-Appadoo, D. A., et al. 2006, MNRAS, 371, 1855

Zhang, B., Zhu, M., Wu, Z.-Z., et al. 2021, MNRAS, 503, 5385

Zhang, C.-P., Xu, J.-L., Wang, J., et al. 2021, arXiv:2111.11018

Zhang, K., Wu, J., Li, D., et al. 2019, SCPMA, 62, 959506

Zhang, K., Wu, J., Li, D., et al. 2020, MNRAS, 500, 1741

Zwaan, M. A., Meyer, M. J., & Staveley-Smith, L. 2010, MNRAS, 403, 1969

Zwaan, M. A., Meyer, M. J., Staveley-Smith, L., & Webster, R. L. 2005, MNRAS: Letters, 359, L30